Data-driven product-process optimization of N-isopropylacrylamide microgel flow-synthesis

Kaven, Luise F.; Schweidtmann, Artur M.; Keil, Jan; Israel, Jana; Wolter, Nadja; Mitsos, Alexander

DOI
10.1016/j.cej.2023.147567

Publication date
2024

Document Version
Final published version

Published in
Chemical Engineering Journal

Chemical Engineering Journal 479 (2024) 147567

Contents lists available at ScienceDirect

Chemical Engineering Journal

journal homepage: www.elsevier.com/locate/cej

Data-driven product-process optimization of N-isopropylacrylamide microgel flow-synthesis

Luise F. Kaven [a], Artur M. Schweidtmann [b], Jan Keil [a], Jana Israel [a], Nadja Wolter [c,d], Alexander Mitsos [a,e,*]

[a] Process Systems Engineering (AVT.SVT), RWTH Aachen University, Forckenbeckstr. 51, 52074 Aachen, Germany
[b] Department of Chemical Engineering, Delft University of Technology, Van der Maasweg 9, 2629 HZ Delft, The Netherlands
[c] DWI - Leibniz Institute for Interactive Materials e.V., Forckenbeckstr. 50, 52074 Aachen, Germany
[d] Functional and Interactive Polymers, Institute of Technical and Macromolecular Chemistry, RWTH Aachen University, Forckenbeckstr. 50, 52074 Aachen, Germany
[e] JARA-soft, RWTH Aachen University, Templergraben 55, 52056 Aachen, Germany

ARTICLE INFO

Dataset link: https://doi.org/10.18154/RWTH-2023-05551

Keywords:
Microgel synthesis
Flow-chemistry
Bayesian optimization
Product-process optimization

ABSTRACT

Microgels are cross-linked, colloidal polymer networks with great potential for stimuli-response release in drug-delivery applications, as their small size allows them to pass human cell boundaries. For applications with specified requirements regarding size, producing tailored microgels in a continuous flow reactor is advantageous because the microgel properties can be controlled tightly. However, no fully-specified mechanistic models are available for continuous microgel synthesis, as the physical properties of the included components are only studied partly. To address this gap and accelerate tailor-made microgel development, we propose a data-driven optimization in a hardware-in-the-loop approach to efficiently synthesize microgels with defined sizes. We optimize the synthesis regarding conflicting objectives (maximum production efficiency, minimum energy consumption, and the desired microgel radius) by applying Bayesian optimization via the solver "Thompson sampling efficient multi-objective optimization" (TS-EMO). We validate the optimization using the deterministic global solver "McCormick-based Algorithm for mixed-integer Nonlinear Global Optimization" (MAiNGO) and verify three computed Pareto optimal solutions via experiments. The proposed framework can be applied to other desired microgel properties and reactor setups and has the potential of efficient development by minimizing number of experiments and modeling effort needed.

1. Introduction

The microgels' size and their ability to react reversibly to external stimuli of temperature, pH, or electrical potential in the surrounding medium [1] is highly relevant for their application. By definition microgels of any form exhibit an equivalent diameter between 0.1 µm to 100 µm in the swollen state [2]. The relevance of the microgel size has been studied for biomedical [3–5], phase separation [6–8], and catalysis [9] applications. Especially smaller microgels (diameters between 0.1 µm to 0.2 µm in the swollen state) have previously been applied for biomedical purposes, e.g., for drug delivery agents for medical uptake and release [4,5] or implant coating [3]. In biomedical applications, microgels are particularly relevant, as their small size allows them to pass the human cell boundary [4]. For the cellular uptake, it was found that microgels of a hydrodynamic radius in the swollen state (at 20 °C) above 400 nm and a cross-linker content above 10 mol% prevent microgel internalization.

The synthesis of microgels in flow reactors can overcome shortcomings of batch reactors, e.g., limited production capacity and downtime between batches, and enhances product development, intensifies production, and facilitates reaction scale-up [10–13]. Furthermore, including process analytical technology in flow reactors allows in-line monitoring and process control under highly reproducible conditions [12–14]. Thus, continuous production enables the reliable synthesis of microgels.

To unfold the full potential of microgels, accelerating the development of tailor-made microgels is desirable. A faster development can be achieved by producing microgels in a continuous reactor mode, as it simplifies up-scaling to large-scale industrial production. Furthermore, model-based approaches facilitate the optimization of microgels with tailored properties. Computational models for describing microgel growth during the synthesis are very sparse and comprise

* Correspondence to: Forckenbeckstr. 51, 52074 Aachen, Germany
E-mail address: amitsos@alum.mit.edu (A. Mitsos).

https://doi.org/10.1016/j.cej.2023.147567
Received 23 September 2023; Received in revised form 3 November 2023; Accepted 19 November 2023
Available online 22 November 2023

mechanistic models suited for batch reaction exclusively [15–20]. Our previous study [13] revealed significant deviations between the reaction progress in batch and flow reactors in the microgel synthesis. In particular, we cannot transfer the batch model equations straight to a plug-flow model, but rather we must consider diffusion effects, temperature distribution, and rheological aspects. The physical properties such as diffusivity coefficient and viscosity are not known during the microgel synthesis, so mechanistic modeling of the flow process is restricted.

To address this gap, we propose a data-driven hardware-in-the-loop optimization for N-isopropylacrylamide-based microgels, one of the most widely studied thermo-responsive microgel systems. The data-driven approach facilitates the reaction optimization of the microgel synthesis in flow. We apply Thompson sampling efficient multi-objective optimization (TS-EMO) [21] to enhance the experimental synthesis design iteratively. The TS-EMO solver is based on the Thompson sampling [22] algorithm, a popular approach in Bayesian optimization. In the following, we present a concise introduction to Bayesian optimization focusing on the TS-EMO algorithm. For a more comprehensive elaboration of the methodology, we kindly direct the interested reader to consult the relevant literature [23,24].

Bayesian optimization searches for a (global) optimum with a focus on efficiency, i.e., aiming for small number of function evaluations. Efficiency is crucial when function evaluations are costly, e.g., require experimentation or extensive computation. In Bayesian optimization, a probabilistic model (also called surrogate or digital twin) of the objective function is constructed and iteratively updated as new data points are evaluated. The surrogate models are constructed via Gaussian Processes (GPs). GPs are considered an effective surrogate model as they provide predictions and variance estimates while relying on relatively few data points [25]. Black-box optimization involving GPs for chemical synthesis has been successfully applied for various reactions [26], including pharmaceutical product development [27], electrochemical reductive carboxylation [28], and polymerization [29]. Based on the surrogate model, a new set of input conditions is proposed for the next experimentation while considering the exploration-exploitation trade-off. The goal is to find the input variable values that minimize the objective function. TS-EMO extends the Thompson sampling algorithm to the multi-objective optimization setting. The promising performance of TS-EMO concerning data efficiency, capacity to handle noise, and the ability for batch-sequential usage [21] makes the algorithm suitable for the optimization of microgel synthesis.

As the microgel size is a highly relevant product characteristic in the mentioned applications, we aim to produce microgels of a targeted size (product feature). Simultaneously, we optimize the product flow and energy demand (process features) because the synthesis has to meet economic and ecological requirements. The synthesis procedure highly influences the characteristics of microgels, and multiple influences on the microgel size have been discovered experimentally. The surfactant [7,10,30–34], monomer [35], cross-linker [31,36–38], and initiator [35,39,40] concentration in the synthesis impact the microgel size. Also, the process conditions, including reactor temperature [31, 35] and flow profile [11,35], determine the microgel size. For the synthesis of microgels with constant cross-linking fraction, we include the reaction temperature, initiator and monomer flow, and the surfactant concentration as variable inputs in our data-driven study.

Since TS-EMO is a stochastic optimization algorithm, it does not guarantee finding the global optimum. We therefore conduct a computational validation step via global deterministic optimization using our open-source software MAiNGO (McCormick-based Algorithm for mixed-integer Nonlinear Global Optimization) [41]. MAiNGO has been demonstrated to be very suitable for optimization with GPs embedded [42]. The global deterministic optimization ensures that for a given GP and acquisition function the optimal solution is found. The computed Pareto-optimal solutions are computed based on the GPs trained on the experimental data. Thus, the Pareto-optimal points are estimates and need to be validated experimentally to show that we are truly able to synthesize the desired microgel and to ensure that computational prediction and real experiment agree. Therefore, in addition, we validate our optimization results experimentally. We conduct the proposed synthesis of a selection of Pareto-optimal points and compare the experimental outcome to the computed findings.

We structure the remaining manuscript as follows. Section 2 describes the experimental setup of the microgel synthesis in the flow reactor. Section 3 reports our optimization approach, including the TS-EMO algorithm, the initial data set, and the problem setup using MAiNGO. Section 4 presents the results of the optimization studies and the computational and experimental validation. Finally, we conclude our work in Section 5.

2. Experimental

2.1. Materials

N-isopropylacrylamide (NIPAM) (97%, ITC Chemicals) is recrystallized from hexane. 2,2'-azobis(2-methylpropionamidine)dihydrochloride (AMPA) (97%, Sigma-Aldrich), *N*, *N*'-methylenebis(acrylamide) (BIS) (99%, Sigma-Aldrich), and hexadecyltrimethylammonium bromide (CTAB) (≥97%, Merck) are used as received. Deionized water (referred to as water) is produced in-house (conductivity $0.8\,\mu S\,cm^{-1}$ at 25 °C).

2.2. Microgel synthesis in flow reactor

We synthesized microgels via precipitation polymerization inside a tubular glass reactor setup, as described in detail in our previous publication [13]. In the following, we provide a brief summary of this experimental setup. Two feed solutions are created, where the monomer and initiator are dissolved in water. The monomer solution contains deionized water with $110.6\,mmol\,L^{-1}$ of NIPAM, $2.7\,mmol\,L^{-1}$ of cross-linker BIS, and $0.41\,mmol\,L^{-1}$ of surfactant CTAB. Thus, the resulting microgels contain a cross-linker fraction of 2.5 mol%. The initiator solution comprises deionized water with $1.5\,mmol\,L^{-1}$ of initiator AMPA. Both solutions (initiator and monomer) and constantly degassed using nitrogen. The flow rates of the monomer and initiator solution can be controlled between $2\,mL\,min^{-1}$ to $18\,mL\,min^{-1}$ and $0.1\,mL\,min^{-1}$ to $0.9\,mL\,min^{-1}$, respectively. Hence, the overall flow rate and the ratio between both feed flows can be adapted. An external heating bath heats the reactor to reaction temperature. We adjust the reactor temperature between 60 °C to 80 °C. The produced microgels exit the reactor, and the solution is cooled to stop the reaction. During the continuous synthesis, we use Raman spectroscopy to determine the weight fraction of the remaining NIPAM (w_{NIPAM}) via in-line measurements. Raman spectra are recorded in HoloGRAMS (Kaiser Optical Systems, Ann Arbor, Michigan, USA) with cosmic ray correction using an RXN2 Raman Analyzer (Kaiser Optical Systems) and an acquisition time of 40 s. More details on the Raman measurement configuration are described in our previous work [13]. We assess the Raman spectra using an evaluation model based on Indirect Hard Modeling [43], which we previously developed [13]. We published the calibration measurements for the model development for transparency and reproducibility [44]. In an off-line step, we use the Zetasizer Ultra (Malvern Panalytical, Malvern, UK) to determine the hydrodynamic diameter (D_H) of the collapsed microgels via Dynamic Light Scattering (DLS). The microgel samples are diluted in ultrapure water and prepared in a disposable capillary cell of the type DTS0012 for the DLS measurements. The measurements are carried out at 50 °C with an angle of 90° (side scatter). For consistency, we acquire microgel size measurements in the collapsed state above the volume phase transition temperature (approximately 32 °C [1]), as the in-line Raman measurements are also conducted at reaction temperature (between 60 °C to 80 °C). For the sake of completeness, we took DLS measurements at 20 °C, which we also provide in the data

Table 1
Bounds on input variable values.

Variable	Unit	Lower bound	Upper bound
F_I	mL min^{-1}	0.1	0.9
F_M	mL min^{-1}	2	18
c_{CTAB}	mmol L^{-1}	0.14	0.41
T	°C	60	80

publication to this work [45]. Each DLS measurement is repeated four times, and the software ZS Xplorer analyzes the results. We exclude experimental data points where the DLS measurements are unreliable due to a high relative error of the microgel size (above 3.8%) or an increased polydispersity index (above 0.6), indicating that no microgels formed. Furthermore, in two cases, undesired hydrogels were produced under the considered experimental settings (see Supporting Information Sec. 3).

3. Computational

The following section is structured as follows. First, we formulate the optimization problem considering the goals and limitations of the experimental setup, see Section 3.1. In Section 3.2, we describe the procedure for generating a set of experiments to initialize the iterative optimization study. Next, we outline the conducted optimization studies in a high-level description in Section 3.3. Further, we give details on the basic operating principle of the employed TS-EMO algorithm in our hardware-in-the-loop setup and the validation approach via global deterministic optimization and the optimization problem definition therein in Sections 3.3.1 and 3.3.2, respectively.

3.1. Optimization problem definition

The optimization aims to find optimal settings for the synthesis to generate a high product output at short residence times and precise, targeted microgel sizes while minimizing the reaction temperature at steady-state. Bayesian optimization designs the best combination of input values to optimize these objectives efficiently. Furthermore, the objectives must be determined from outputs quantifiable via established monitoring techniques.

The reaction system has four optimization variables as inputs $\mathbf{x}$: reaction temperature T, surfactant concentration c_{CTAB}, and flow rates of the initiator F_I and monomer F_M solution. The bounds on the inputs are presented in Table 1. The range of T comprises the minimum of 60 °C when the initiator decomposition effectively sets in [46] and the maximum of 80 °C when solvent evaporation becomes an issue. The bounds on c_{CTAB} are based on the reaction experience that no colloidal stability sets in below the lower limit. Generally, a higher c_{CTAB} causes a smaller microgel size. Thus, we determined the upper limit for c_{CTAB} based on preliminary experiments. The pump's capacity defines the limits for the monomer and initiator solution flow rates. Furthermore, at the minimum $F_M = 2\,\mathrm{mL\,min^{-1}}$, which entails the maximum residence time in the reactor (approximately 1800 s), the final conversion is reached, as discovered in our previous work [13]. The employed upper bounds allow for achieving the desired microgel size range, as we conclude from empirical knowledge. The concentration of the monomer NIPAM ($c_{NIPAM} = 110.6\,\mathrm{mmol\,L^{-1}}$) in the stock solution, and the ratio of monomer to cross-linker BIS are kept constant for the reaction optimization to maintain a cross-linking fraction of 2.5 mol% within the microgel.

We measure two quantities of the system at the end of the reaction: The weight fraction of the monomer NIPAM w_{NIPAM} and the microgel's hydrodynamic radius r_H. From the measurements, we derive two quantities $\mathbf{y}$ for the surrogate model data set: The product flow ($F_{Product}$) and the squared deviation from the targeted microgel size (Δr_H^2). The product flow characterizes the reactor efficiency and is computed via:

$$F_{Product} = \frac{w_{NIPAM,0} - w_{NIPAM,f}}{w_{NIPAM,0}} \cdot (F_I + F_M),$$

where $w_{NIPAM,0}$ and $w_{NIPAM,f}$ denote the initial and final NIPAM weight fraction.

The output Δr_H^2 is calculated as the squared difference between the measured and targeted hydrodynamic radius:

$$\Delta r_H^2 = (r_{H,measured} - r_{H,target})^2.$$

The targeted microgel size in this contribution is a hydrodynamic radius of 100 nm in the collapsed state at 50 °C, as the size range is relevant in medical applications to pass the human cell boundary. Previously, it was found that microgels with a hydrodynamic diameter above 800 nm in the swollen state are unsuitable for cellular uptake [4]. This size corresponds to a hydrodynamic radius of approximately 222 nm at the collapsed state. Thus, microgels of a hydrodynamic radius of 100 nm are expected to achieve fast cellular uptake kinetics.

The efficient microgel production targets a low reaction temperature as heating contributes significantly to energy consumption. The reaction temperature T is an input to the reactor system; hence, no additional measurement technology is needed. The difference to the minimum allowable temperature (see Table 1) is defined as another objective function:

$$\Delta T = T - T_{min}.$$

Technically, the input temperature can be used as an objective function directly. However, we use the temperature difference as the objective to scale the temperature values to a similar magnitude as the flow rates and to underline the generality of the method.

The resulting multi-objective optimization problem is summarized in the following:

$$\min_{\mathbf{x}\in[\mathbf{x}^L,\mathbf{x}^U]} -F_{Product},\ \Delta r_H^2,\ \Delta T,$$

where, $\mathbf{x} = [F_I, F_M, c_{CTAB}, T]$, and $\mathbf{x}^L$ and $\mathbf{x}^U$ denote their corresponding lower and upper bounds as presented in Table 1.

3.2. Initial data set

Effective initial values are important to initialize the data-driven optimization algorithm. Often random choices are taken as initial guesses, without distinguishing between variables. However, we aim for efficient usage of experimental resources and accordingly devised the following tailored initialization. We configure three groups of experiments, each comprising five experimental settings. The division is visualized in Fig. 1. We distinguish between input variables T and c_{CTAB} that are at a fixed value for each group and inputs F_M and F_I that vary simultaneously within one group. We adopt a group size of five experimental settings per session, as this quantity aligns with the capacity of a day's work in the laboratory.

Furthermore, we decided to consider three groups of experiments as a trade-off between covering the input space of T and c_{CTAB} sufficiently and conducting a reasonable size of initial experiments in total.

Changing T between experimental runs relates to long transition times. Thus, we keep T at a fixed value for each group of experiments for an efficient proceeding. Also, c_{CTAB} is fixed for an experimental group, as preparing the monomer solution with different content of CTAB for each experiment execution is laborious and increases the risks of inserting air into the reactor system (oxygen inhibits the reaction) while decreasing the flexibility of the reaction setup. Therefore, keeping c_{CTAB} fixed constitutes a trade-off between effort for the synthesis preparation, risk of contamination, and loss of flexibility in synthesis execution.

We employ the `lhsdesign` function for Latin Hypercube Sampling (LHS) in MATLAB 2019b to determine the input values for the initial

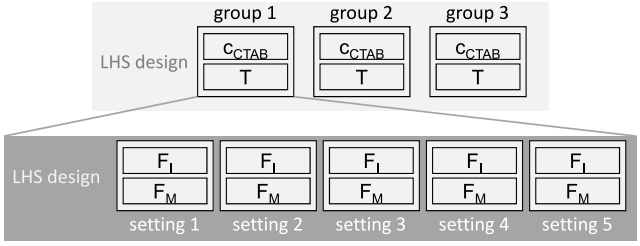

Fig. 1. Grouping of initial experiments designed via LHS.

experiments. In the first step, we set the values for T and c_{CTAB} for each of the three groups via LHS. Subsequently, we perform LHS again for F_I and F_M within each group for five settings. In total, we derive an amount of 15 initial experiments.

3.3. General approach

We conduct a hardware-in-the-loop optimization study involving TS-EMO and a validation study including computational and experimental validation. In the hardware-in-the-loop approach, we employ TS-EMO to determine the next group of experiments based on an initial experimental data set. The Bayesian optimization algorithm TS-EMO iteratively suggests new experimental conditions based on the results of previous experiments. After the suggested group conditions are experimentally tested, we repeat the optimization process and subsequent experimentation until eleven iterations have been reached. Finally, we validate the results from the TS-EMO study computationally via global deterministic optimization using the software MAiNGO and experimentally with reaction settings from Pareto optimal points.

3.3.1. TS-EMO algorithm

We apply TS-EMO [21] to the product-process optimization of the continuous microgel synthesis. The schematic setup of the reactor combined with the algorithm is shown in Fig. 2. TS-EMO uses experimental data points $\mathbf{x}^{(i)} = [F_I, F_M, c_{CTAB}, T]$ and $\mathbf{y}^{(i)} := [F_{product}, \Delta r_H^2]$ to create an approximation via a GP surrogate model of the unknown function f. For the training of the GPs, we apply Matérn type 1 as the function kernel. The third objective can directly be calculated from the input variables. In the multi-objective optimization step, Thompson sampling allows approximating the Pareto set of the optimal solutions. Here, we set the number of spectral sampling points to 4,000. Lastly, an optimal candidate set of input conditions $\mathbf{x}^{(i+1)} = [F_{I,new}, F_{M,new}, c_{CTAB,new}, T_{new}]$ is calculated to continue in the next experimental iteration loop. The settings incorporate a genetic algorithm with 1,000 generations for optimization.

In conclusion, the TS-EMO algorithm is provided with an initial experimental data set designed via LHS. The algorithm then provides a new set of experiments to be conducted in the following experimental round. Subsequently, in each optimization round, we determine a set of the following five experiments at one fixed T and c_{CTAB} with varying F_I and F_M. We chose batch-sequential optimization, meaning evaluating multiple points in each iteration, as off-line DLS measurements are conducted more efficiently in batch preparation. In addition, we chose five experimental settings, as we can adequately conduct this quantity within one day of synthesis experimentation. The TS-EMO calculation and the experimentation are repeated in multiple iterations. Meanwhile, searching for the optimal recipe should take as few iterations as possible to decrease the experimental effort and expense of chemicals used. Thus, the hardware-in-the-loop procedure ends when a certain number of iterations have been performed or the executor decides that sufficient reaction knowledge has been gathered. In the presented study, we end the procedure after eleven iterations.

3.3.2. Global deterministic optimization

For the computational validation, we use MAiNGO [41] to conduct a global deterministic optimization. We employ MAiNGO as an alternative approach to the non-deterministic optimization included in the TS-EMO algorithm. Validation using MAiNGO does not require conducting new experiments but leverages the data collected during the Bayesian optimization. For the validation study, $F_{Product}$ acts as the single objective. Additionally, we apply the ϵ-constraint method [47] to restrict the objective Δr_H^2. As the remaining objective ΔT is directly proportional to the input T, we restrict the upper bound of the input variable T step-wise. For the global optimization, we use the experimental data received in the TS-EMO study and do not perform further experiments in the form of a hardware-in-the-loop approach. We set the starting point and the ϵ values for the optimization based on the results derived from the hardware-in-the-loop study.

We rewrite the optimization problem to a single-objective formulation in reduced space:

$$\begin{aligned} \min_{\mathbf{x}\in[\mathbf{x}^L,\mathbf{x}^U]} \; & -F_{Product} \\ \text{s.t. } & \Delta r_H^2 \le \epsilon \end{aligned} \tag{1}$$

As stated above, the values for ϵ, $\mathbf{x}^U$ of T, and the starting point are derived from the results of the TS-EMO study.

4. Results and discussion

The results and discussion are organized as follows. First, we present our findings from the study involving TS-EMO with four inputs and three objectives in Section 4.1. There we show the Pareto optimal solutions for the three-dimensional objective system, the progression of the experimental outcome with accumulating experimentation, the error analysis of the measurements, and the Pareto optimal solutions for each of the four inputs. Subsequently, we display the results of the validation studies in Section 4.2. The computational validation via global deterministic optimization is shown in Section 4.2.1. We reformulated the optimization problem to a single objective with four input variables for the final study. In Section 4.2.2, we additionally exhibit the experimental validation of three Pareto optimal points. We provide all experimental data [45]. The data includes the raw Raman measurements and an evaluation of the DLS measurements. In addition, we make data points underlying the graphical representation of the results available in Supporting Information Sec. 2. The data points include the experimental data (Supporting Information Section 2.1) and the Pareto optimal solutions calculated via global deterministic optimization in the validation step (Supporting Information Sec. 2.2). As the Pareto optimal solutions calculated via TS-EMO are exhaustive, the data is not provided explicitly. The results can be re-constructed by applying TS-EMO on the experimental data provided. The software employed in this contribution is available open-source: TS-EMO [48] and MAiNGO [49] with MeLOn [50], the interface for embedded machine-learning models.

4.1. Hardware-in-the-loop involving TS-EMO

We conduct eleven iterations for the hardware-in-the-loop optimization. We analyze the Pareto optimal solutions in detail regarding the feasible space of the objective values in Section 4.1.1. Next, the progression of the experimentation outcome, an analysis of the errors from the experimental measurements, and the computational uncertainty of the calculated Pareto front are presented in Section 4.1.2. Lastly, we evaluate the input variable values at the Pareto optimal points to derive suitable reactor settings for the desired microgel product in Section 4.1.3.

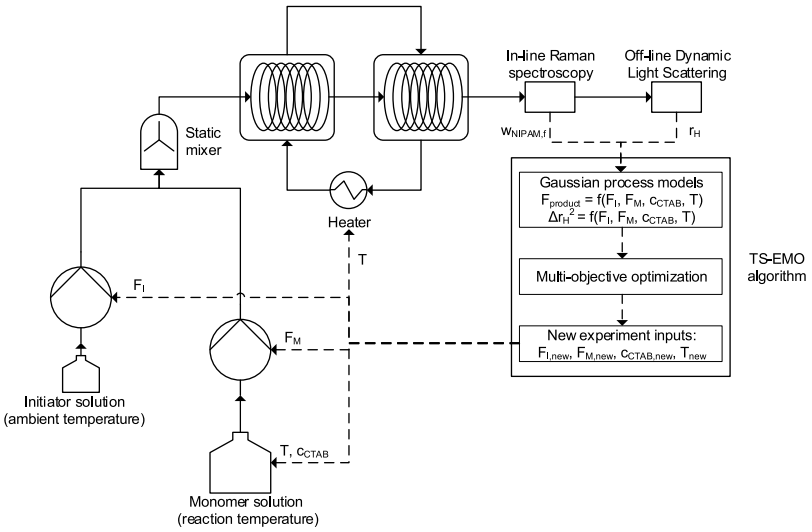

Fig. 2. Overview of the iterative multi-objective optimization of the microgel synthesis in flow using the TS-EMO algorithm. Solid arrows indicate material flow, dotted arrows represent information transfer.

4.1.1. Pareto optimal solutions

In the hardware-in-the-loop study, F_I, F_M, c_{CTAB}, and T are varied as the inputs to the reactor, and $F_{Product}$, Δr_H^2, and ΔT are the objectives. Fig. 3 shows the resulting Pareto front of the study calculated using TS-EMO (marked with colored circles) and the experimental data points obtained during the hardware-in-the-loop optimization (marked with 'x' symbols). Later, in Section 4.1.2, we will also show the progression of experimental outcomes for each iteration separately (see Fig. 4). For the TS-EMO calculations in Fig. 3, we used a population size of 5,000 to represent the three-dimensional Pareto front sufficiently. As visualizing three objectives is challenging, we proceed with a two-dimensional plot and add a color scale for the third objective to visualize the estimated Pareto front for better interpretation. However, it is crucial to remember that we are considering three-dimensional optimization results for the meaningful interpretation of the two-dimensional plots.

For the two-dimensional Pareto fronts, the desired outcome in Fig. 3, the utopia point, of the multi-objective optimization regarding the product flow and the squared radius deviation is located in the bottom left corner of the plot. Equally, small temperature deviations (depicted in dark blue) indicate the location of the utopia point in the third dimension. Looking at the results, it appears that the three objective functions are conflicting; thus, reaching the utopia point is impossible. In other words: the product flow rate becomes lower for microgels closer to the targeted size, and higher temperatures are needed for high product flow rates. In addition, the shaded area around a squared radius deviation accounts for a difference of ±5 nm or 5% to the desired size.

The analysis of the estimated Pareto front in Fig. 3 yields that up to 6.0 mL min^{-1} of product flow, a microgel size sufficiently close (±5 nm) to the desired size is achievable. The microgel size deviation begins to diverge more strongly from the targeted value after a product flow rate of approximately 6.5 mL min^{-1} is reached. This deviation shows that product flow rates above a value of around 6.5 mL min^{-1} are incompatible with the targeted microgel size.

The temperature influences the optimal product flow more significantly than the optimal microgel size. This trend is represented by the color indicated temperature change that is more substantial along the x-axis than the y-axis. The underlying GPs (depicted in Supplementary Information Sec. 1) show that an increase in temperature generally accompanies an increase in product flow. Still, the product flow converges towards approximately 6.5 mL min^{-1} for temperatures above approximately 70 °C (corresponding to 10 K temperature deviation). Thus, low temperatures (below 70 °C) are sufficient considering

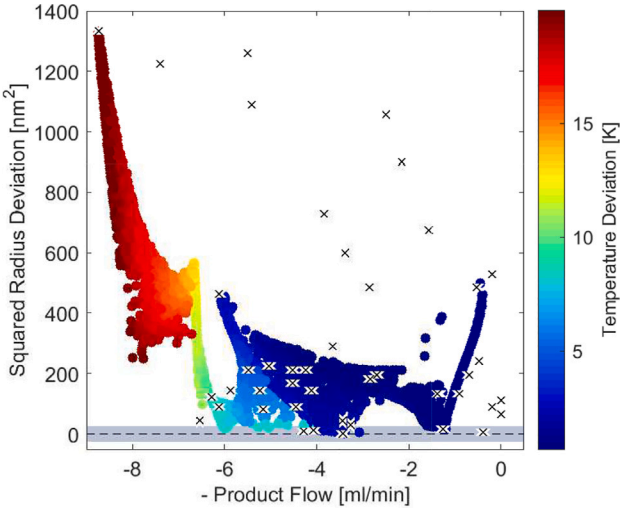

Fig. 3. Estimated Pareto front of the hardware-in-the-loop study using TS-EMO: Squared radius deviation over product flow. The color scale indicates the temperature deviation. The x symbols mark the experimental data points. The shaded area maps the deviation of ±5 nm to the desired microgel radius. (For interpretation of the references to color in this figure legend, the reader is referred to the web version of this article.)

the trade-off between maximizing product flow and achieving the targeted microgel size, as above approximately 70 °C only the product flow improves. Overall, the optimal temperature input spans the entire allowable range between 60 °C to 80 °C. Furthermore, the GP for the squared radius deviation (Supplementary Information Sec. 1) shows an increase with rising temperatures. However, the correlation between reaction temperature and microgel size deviation appears highly non-linear and subject to inherent variance. Lastly, the underlying GP for the temperature deviation (Supplementary Information Sec. 1) confirms the successful training of the GPs, as the temperature deviation shows no correlation to F_I, F_M, or c_{CTAB}, and is directly proportional to the input temperature values with little variance.

In conclusion, the results concerning a suitable microgel size at a high product flow and medium reactor temperatures are promising. The underlying GPs confirm our apriori reaction knowledge; thus, we can validate the functionality of the applied method elementarily. However, the GPs are occasionally subject to high variance, and the available data points are limited. Nevertheless, we can derive meaningful information

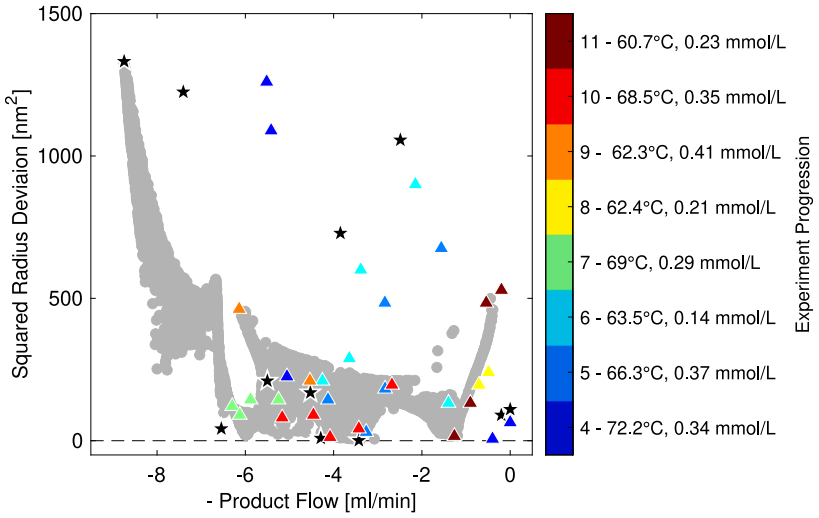

Fig. 4. Estimated Pareto front of the hardware-in-the-loop study using TS-EMO: Squared radius deviation over product flow. The gray circles represent the estimated Pareto optimal solutions based on the GPs. The stars indicate the initial experimental data set and the triangles the subsequent experimental data points, while the color of the triangles shows the experimental progression. (For interpretation of the references to color in this figure legend, the reader is referred to the web version of this article.)

about the synthesis, e.g., limiting the temperature to 70 °C is sufficient for successful synthesis. Furthermore, we find that a maximum product flow of 6.0 mL min^{-1} is achievable when restricting the allowable microgel size deviation to ±5 nm.

4.1.2. Experiment progression and error analysis

In Fig. 4, the calculated Pareto front is shown with the progression of the experimentation. The temperature and the surfactant concentration for each experimental group are listed in addition to the order of experiment progression on the color scale. In the graph, the stars mark the results from the initial experiments designed via LHS. The LHS ensures a good distribution over the input space. The initial experimental results also cover the output space adequately, indicating that the initial data set already provides a reasonable basis for information on the reaction.

Furthermore, the triangles depicted in a color scale represent the experimentally determined data points and their progression in the hardware-in-the-loop approach. In each set of experiments, five data points are received. We must neglect some data points due to DLS measurement showing a high size distribution index (indicating that no real microgel was formed) or a high relative measurement error. Thus, a reduced amount of experimental data points is shown. There is no clear trend visible in the experiment progression, as the algorithm tries to balance exploitation and exploration in the design of the next experiment. The listed temperature and surfactant concentration values along the experimental progression show that the algorithm mostly explores temperature regions below 70 °C. While the surfactant concentration is varied over the entire allowed input space. Also, for the conducted experiments in this study, the algorithm does not repeat in any iteration the suggested experimental conditions regarding the combination of temperature and surfactant concentration. Although output measurements are sometimes excluded without further information to the algorithm, the algorithm does not try to re-evaluate the correlated input space. The batch-sequential procedure presumably achieves that the algorithm carries on without going back to previously tested conditions where no information was received. In other words: although no input information is gathered at certain input conditions within one experimental group, the information from the remaining input conditions within the group supports the algorithm enough.

In Fig. 5, the calculated Pareto front is shown with the computational standard deviation of the optimal points. Also, the experimental data points are depicted with the according experimental error bars.

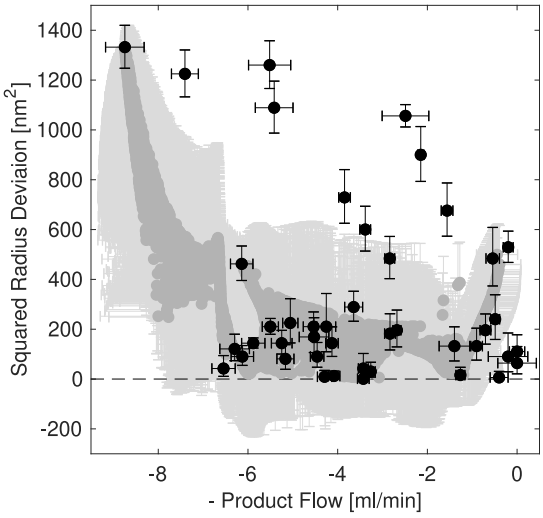

Fig. 5. Estimated Pareto front of the hardware-in-the-loop study using TS-EMO: Squared radius deviation over product flow. The gray circles represent the estimated Pareto optimal solutions based on the GPs and the according standard deviation. The black circles indicate the experimental outcomes and the according measurement uncertainty.

The magnitude of the experimental error is derived from the measurement technology. The evaluation model of the Raman measurements has an inherent root mean squared error of cross-validation (RMSECV) of 0.037 wt-%. The error propagation, including the RMSECV, is considered for the uncertainty of the product flow. For the DLS measurement, the Zetasizer Ultra internally evaluates the standard deviation over the four conducted measurements. This error value is also propagated for the uncertainty of the experimental squared particle size deviation.

Some experimental data points lie slightly below the estimated Pareto front. This phenomenon becomes visible in a three-dimensional analysis. However, the considered experimental data points lie within the calculated standard deviation of the estimated Pareto front for the squared radius deviation. Furthermore, the experimental error bars resulting from the DLS and Raman measurement errors are displayed to underline the magnitude of uncertainty inherent in the real-life experimental setup.

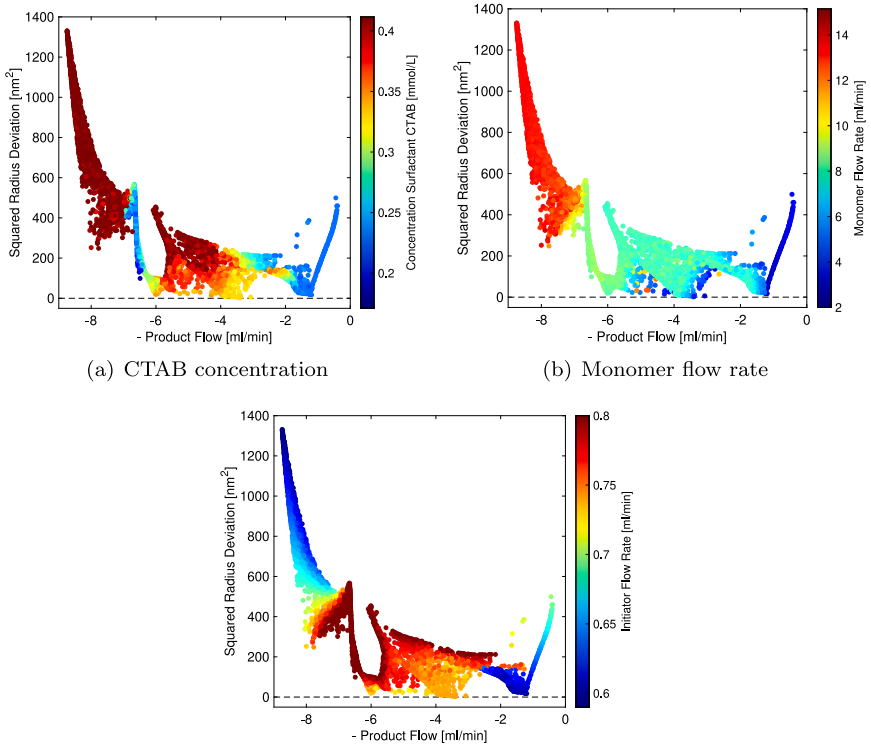

(a) CTAB concentration (b) Monomer flow rate

(c) Initiator flow rate

Fig. 6. Estimated Pareto front of main study: Squared radius deviation over product flow for the input variables (a) CTAB concentration, (b) monomer flow rate, and (c) initiator flow rate. The circles represent the estimated Pareto optimal solutions based on the GPs, while the color scale indicates the magnitude of the respective input variable. (For interpretation of the references to color in this figure legend, the reader is referred to the web version of this article.)

4.1.3. Pareto optimal solutions for different inputs

In Fig. 6(a) to 6(c), the Pareto front for the objectives Δr_H^2 and $F_{Product}$ and three out of the four applied inputs is shown. The color scale indicates the associated input configuration. The inputs pictured include the surfactant concentration, the monomer, and the initiator flow rate. The Pareto front with the according input temperature is not depicted explicitly, as Fig. 3 contains information on the input temperature.

Fig. 6(a) shows that the microgel size deviates strongly from the desired size for higher c_{CTAB} values. Overall, c_{CTAB} ranges only between $0.22\,\mathrm{mmol\,L^{-1}}$ to $0.41\,\mathrm{mmol\,L^{-1}}$. The underlying GP (depicted in Supplementary Information Sec. 1) indicates that the product flow can be considered independent of c_{CTAB}. In contrast, the correlation between squared radius deviation and c_{CTAB} is impaired by high variance. The finding that the product flow is unaffected by c_{CTAB} follows the expected outcome, as a change in stabilizer should not impact the conversion kinetics of the reaction system.

In Fig. 6(b), the monomer flow rate ranges between $2.75\,\mathrm{mL\,min^{-1}}$ to $14.2\,\mathrm{mL\,min^{-1}}$ and mainly correlates to the product flow. The relation between monomer flow rate and product flow is defined in Eq. stating that generally, the monomer flow and product flow are directly proportional (second term in Eq.). However, the monomer flow rate is also related to the conversion (first term of Eq.). A higher monomer flow can cause a smaller conversion, as not all monomer can be consumed in the smaller residence time. The underlying GP (depicted in Supplementary Information Sec. 1) shows the trade-off between high monomer flow rates associated with an increased overall flow and a lower conversion and low monomer flow rates with a low overall flow but higher conversion. Furthermore, the monomer flow rate has little to no influence on the microgel size deviation according to the underlying GP.

Finally, Fig. 6(c) shows the Pareto front for different initiator flow rates. Here, the initiator flow rate ranges between $0.59\,\mathrm{mL\,min^{-1}}$ to $0.8\,\mathrm{mL\,min^{-1}}$ with a clear tendency to the upper bound. Similar to the monomer flow rate, the initiator flow rate is directly proportional to the product flow as defined in Eq. . However, the initiator flow is a maximum of a third of the total flow rate and thus less significant for the overall change in residence time. As expected, the underlying GP (depicted in Supplementary Information Sec. 1) also shows a highly linear correlation between initiator flow rate and product flow. In addition, the GP for the squared radius deviation shows no clear trend depending on the initiator flow rate.

4.2. Validation

The validation conducted within this contribution includes a computational and experimental part. The computational validation is global deterministic optimization of the final GP, Section 4.2.1. The experimental validation is carried out for three calculated Pareto optimal solutions, and the results are shown in Section 4.2.2.

4.2.1. Computational validation via global deterministic optimization

We proceed with a final deterministic global optimization using MAiNGO. The results from the hardware-in-the-loop study are incorporated into the final optimization for validation. First, the data points from the TS-EMO study are used to train GPs for $F_{Product}$ and Δr_H^2. The training settings are the same as for the GPs used in the hardware-in-the-loop approach including TS-EMO. Second, the identified optimal point close to the targeted microgel size and a sufficient product flow at a reasonably low temperature is embedded as the starting point of the optimization: $F_I = 0.73\,\mathrm{mL\,min^{-1}}$, $F_M = 8.1\,\mathrm{mL\,min^{-1}}$, $c_{CTAB} = 0.34\,\mathrm{mmol\,L^{-1}}$, and $T = 68.5\,°\mathrm{C}$. The calculated outcome for these input variables yields a microgel size deviation of $21.1\,\mathrm{nm^2}$ and a product flow of $6.0\,\mathrm{mL\,min^{-1}}$. Also, the visualization of the TS-EMO study (see Fig. 3) allows setting reasonable values for the ϵ constraint method.

For the deterministic global optimization, the results including the ϵ constraint method, are presented in Fig. 7 for each input separately. Here, we constrain the squared radius deviation step-wise with a maximum of 25 nm^2. The problem becomes infeasible, meaning under the specified conditions no solution meets all the constraints and still optimizes the objective, for squared radius deviations below 2 nm^2. We compare the global deterministic optimization (MAiNGO) with the optimization results for two objectives (product flow and squared radius deviation) using TS-EMO.

Overall, the Figs. 7(a) to 7(d) show that the experimental data points, the Pareto front generated via TS-EMO, and the Pareto front obtained from MAiNGO agree correctly above a product flow of approximately 4.3 mL min^{-1}. TS-EMO finds a feasible Pareto optimal solution only down to 12.6 nm^2 at a product flow of 4.0 mL min^{-1}. In this region, the calculated solution via MAiNGO diverges and includes feasible solutions in the product flow range around 4.3 mL min^{-1} with squared radius deviations between 10 nm^2 to 12 nm^2.

The experimental data is obtained through hardware-in-the-loop optimization, balancing exploration and exploitation strategies. Consequently, the experimental data only partly aligns with the computed Pareto curve, as the algorithm also ventures into uncharted regions. Particularly at low product flows with high radius deviations, the experimental points are not part of the Pareto optimal set. However, the calculated Pareto optimal curve relies on the experimental data points. Hence, it becomes imperative that in the region of multi-objective optima, the experimental data points agree with the calculated Pareto front. As illustrated in Fig. 7, the experimental values agree with the calculated results along the estimated Pareto front, implying qualitatively that the result is trustworthy.

Within the Pareto optimal solutions calculated via MAiNGO, three regimes can be differentiated most visible for the CTAB concentration and the reaction temperature. These regimes range at a product flow of 3.4 mL min^{-1} to 3.8 mL min^{-1}, around 4.3 mL min^{-1}, and 4.5 mL min^{-1} to 6 mL min^{-1}. In each regime, the CTAB concentration, the initiator flow rate, and the reaction temperature are approximately constant, and only the monomer flow rate varies.

Further, we change the upper bound of the reactor temperature input variable value to 61 °C, 62 °C, and 70 °C. The results of the TS-EMO optimization with two objectives compared to global deterministic optimization results via MAiNGO are shown in Fig. 8. The problem becomes infeasible for squared radius deviations below 2 nm^2 for temperatures 62 °C and higher, and below 16 nm^2 for 61 °C. In other words, based on the optimization results it is not possible to synthesize microgels with a squared radius deviation below 2 nm^2 when restricting the reaction temperature to a maximum of 62 °C or higher. Similarly, for a maximum temperature of 61 °C, the smallest achievable squared radius deviation is 16 nm^2.

In Fig. 8, the Pareto optimal points generated via TS-EMO and MAiNGO agree mostly. Only for a maximum input temperature of 61 °C the global deterministic optimization via MAiNGO finds slightly better Pareto optimal points for squared radius deviations above 23 nm^2. However, the product flow range between 1.3 mL min^{-1} to 1.6 mL min^{-1} and a minimum squared radius deviation of 16.4 nm^2 for the associated temperature are undesirable. Thus, temperatures above 61 °C are more relevant. For a maximum input temperature of 62 °C, the Pareto optimal product flow is limited to 4 mL min^{-1} even for substantial deviations in squared radius at 25 nm^2. The Pareto optimal points for squared radius deviations below 13 nm^2 overlap for the MAiNGO and TS-EMO optimization for 62 °C and 70 °C. For a maximum input temperature of 70 °C, a notable improvement of the product flow up to approximately 6 mL min^{-1} is achievable when allowing squared radius deviations starting at 18 nm^2 and above. The TS-EMO Pareto optimal points only cover squared radius deviations above 12.5 nm^2 for a maximum temperature of 70 °C. The Pareto optimal points for the MAiNGO optimization with a maximum temperature of 70 °C (Fig. 8) and 80 °C (Fig. 7) agree except for the regime around 4.3 mL min^{-1} and squared radius deviations of 10 nm^2 to 12 nm^2 indicating that temperatures above 70 °C are irrelevant for optimized reactor settings.

Table 2
Experimental validation of global deterministic optimization.

Experiment	Input	Value	Output	Estimated value	Experimental value
1	T	68.5 °C			
	c_{CTAB}	0.35 mmol L^{-1}	$F_{Product}$	5.95 mL min^{-1}	5.93 mL min^{-1}
	F_I	0.73 mL min^{-1}	Δr_H^2	17 nm^2	100 nm^2
	F_M	7.69 mL min^{-1}			
2	T	71.0 °C			
	c_{CTAB}	0.16 mmol L^{-1}	$F_{Product}$	4.29 mL min^{-1}	4.20 mL min^{-1}
	F_I	0.34 mL min^{-1}	Δr_H^2	10 nm^2	12.25 nm^2
	F_M	4.87 mL min^{-1}			
3	T	62.0 °C			
	c_{CTAB}	0.33 mmol L^{-1}	$F_{Product}$	3.43 mL min^{-1}	3.53 mL min^{-1}
	F_I	0.74 mL min^{-1}	Δr_H^2	2 nm^2	2.25 nm^2
	F_M	3.68 mL min^{-1}			

Overall, the Pareto optimal solutions of TS-EMO and MAiNGO agree very well. Hence, the hardware-in-the-loop procedure using TS-EMO is validated sufficiently. However, the global deterministic optimization finds feasible Pareto optimal solutions beyond TS-EMO. The global deterministic optimization of the multi-objective synthesis problem is beneficial because little data is available, and thus guaranteeing a reliable and reproducible solution is crucial. However, the surrogate models represented by GPs are subject to significant variance. Thus, a solution representing the actual reality remains challenging. We also demonstrate that the deterministic single-objective formulation is advantageous here to focus on the output space of interest and reduce computational effort.

4.2.2. Experimental validation

We conduct three experiments along the deterministically estimated Pareto front for an experimental validation step to determine if the computed estimate based on the trained GPs can be verified experimentally. The inputs, the estimated, and experimentally determined values are presented in Table 2. The experimental and calculated values agree very well for the product flow. The most significant difference regarding the product flow occurs in Experiment 3 with an absolute divergence of 0.03 mL min^{-1} (or approximately 2.8%) to the calculated value. Generally, the agreement of calculated and experimental values is higher for the product flow than for the squared radius deviation. The most notable difference regarding the squared radius deviation arises for Experiment 1, where the absolute divergence is 83 nm^2. This significant divergence can be attributed to the high variation in the GP prediction for the squared radius deviation. At the same time, the estimated and experimental value for Experiments 2 and 3 agree sufficiently. Experiment 3 shows that we can efficiently synthesize microgels with a radius of 101.5 nm, which is acceptable in terms of accuracy.

Overall, the experimental validation indicates that the obtained data is enough to enable an adequate prediction via a GP surrogate model. The agreement between estimated and calculated data is good, although the underlying GPs are subject to significant variance. The applied procedure is successful with an absolute deviation of 1.5 nm to the desired microgel radius.

5. Conclusions

Polymerization reactions in flow reactors play an essential role in precise polymer production. The efficient, accurate, reproducible synthesis of polymers such as microgels is important. Data-driven optimization supports the microgel development effectively. We incorporate the multi-objective optimization algorithm TS-EMO to optimize the synthesis of tailored microgels ecologically and economically. The proposed

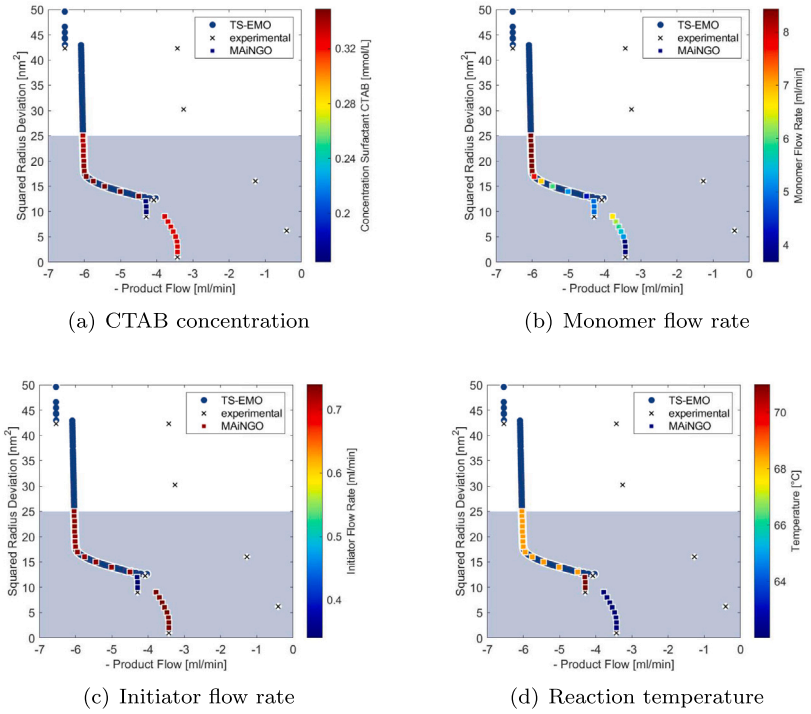

Fig. 7. Estimated Pareto front of global deterministic optimization: squared radius deviation over product flow for the input variables (a) CTAB concentration, (b) monomer flow rate, (c) initiator flow rate and, (d) reaction temperature. The squares represent the estimated Pareto optimal solutions based on the GPs, while the color scale indicates the magnitude of the respective input variable. The x symbols mark the experimental data points. The blue circles indicate the estimated Pareto front via TS-EMO for two objectives only. (For interpretation of the references to color in this figure legend, the reader is referred to the web version of this article.)

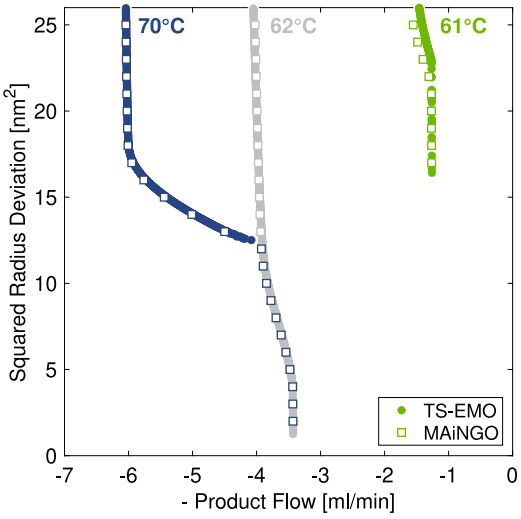

Fig. 8. Comparison of TS-EMO and MAiNGO results for different bounds on input temperature. The filled circles represent the Pareto optimal points calculated via TS-EMO, while the squares show the Pareto optimal points calculated via MAiNGO.

synthesis settings enable a product flow of maximum 6.0 mL min^{-1} while remaining in an acceptable range of ±5 nm to the targeted hydrodynamic radius. We use the global deterministic optimization software MAiNGO to prove the reliability and reproducibility of the results. In addition, we demonstrate the usefulness of global deterministic solutions for problems with little data availability.

From the experimental side, including Raman spectroscopy constitutes a powerful in-line process analytical tool that has the potential to be incorporated into automated reaction optimization setups. Limitations of the proposed work include the non-automated reactor system due to off-line DLS measurements. Dependable in-line size determination remains a critical shortcoming on the road to autonomous reaction optimization. Furthermore, the DLS data is occasionally unreliable or shows a high polydispersity (indicating no real microgel is produced). Angle-dependent DLS measurements could be incorporated in future works to exploit the ability of DLS to analyze polydispersity and secondary particle formation. At the moment, these data points are discarded but could be meaningfully included as valuable information for the algorithm in the future. The reliability of DLS data and the challenging interpretation of the GP predictions shows that expert knowledge is still crucial in the optimization procedure and limits a potentially autonomous process based on machine learning. Generally, data-driven optimization is limited to a specific reactor setup. However, we can quickly adapt the proposed framework to other desired microgel properties and reactor setups. Thus, this work supports and enhances the development of suitable microgels for size-specific applications. The presented method efficiently explores new microgel synthesis recipes that facilitate tailor-made microgel production.

Declaration of competing interest

The authors declare that they have no known competing financial interests or personal relationships that could have appeared to influence the work reported in this paper.

Data availability

https://doi.org/10.18154/RWTH-2023-05551.

Acknowledgments

This work was performed as a part of project B4 of theCRC 985 “Functional Microgels and Microgel Systems” funded by Deutsche Forschungsgemeinschaft (DFG). The authors thank Jan Steinstraßen for

support with conducting continuous microgel syntheses. The authors also thank Johannes M. M. Faust for fruitful discussions and Jannik Lüthje and Daniel Jungen for support with the software MAiNGO.

Appendix A. Supplementary data

Supplementary material related to this article can be found online at https://doi.org/10.1016/j.cej.2023.147567.

References

[1] A. Pich, W. Richtering, Chemical Design of Responsive Microgels, Vol. 234, Springer Berlin Heidelberg, Berlin, Heidelberg, 2011, http://dx.doi.org/10.1007/978-3-642-16379-1.

[2] J.V. Alemán, A.V. Chadwick, J. He, M. Hess, K. Horie, R.G. Jones, P. Kratochvíl, I. Meisel, I. Mita, G. Moad, S. Penczek, R.F.T. Stepto, Definitions of terms relating to the structure and processing of sols, gels, networks, and inorganic-organic hybrid materials (IUPAC recommendations 2007), Pure Appl. Chem. 79 (10) (2007) 1801–1829, http://dx.doi.org/10.1351/pac200779101801.

[3] D. Keskin, O. Mergel, H.C. van der Mei, H.J. Busscher, P. van Rijn, Inhibiting bacterial adhesion by mechanically modulated microgel coatings, Biomacromolecules 20 (1) (2019) 243–253, http://dx.doi.org/10.1021/acs.biomac.8b01378.

[4] V.K. Switacz, S.K. Wypysek, R. Degen, J.J. Crassous, M. Spehr, W. Richtering, Influence of size and cross-linking density of microgels on cellular uptake and uptake kinetics, Biomacromolecules 21 (11) (2020) 4532–4544, http://dx.doi.org/10.1021/acs.biomac.0c00478.

[5] C. Zhang, E. Gau, W. Sun, J. Zhu, B.M. Schmidt, A. Pich, X. Shi, Influence of size, crosslinking degree and surface structure of poly(N-vinylcaprolactam)-based microgels on their penetration into multicellular tumor spheroids, Biomater. Sci. 7 (11) (2019) 4738–4747, http://dx.doi.org/10.1039/c9bm01132c.

[6] M. Faulde, E. Siemes, D. Wöll, A. Jupke, Fluid dynamics of microgel-covered drops reveal impact on interfacial conditions, Polymers 10 (8) (2018) http://dx.doi.org/10.3390/polym10080809.

[7] M. Destribats, M. Eyharts, V. Lapeyre, E. Sellier, I. Varga, V. Ravaine, V. Schmitt, Impact of pNIPAM microgel size on its ability to stabilize pickering emulsions, Langmuir : ACS J. Surf. Colloids 30 (7) (2014) 1768–1777, http://dx.doi.org/10.1021/la4044396.

[8] W. Richtering, Responsive emulsions stabilized by stimuli-sensitive microgels: Emulsions with special non-Pickering properties, Langmuir : ACS J. Surf. Colloids 28 (50) (2012) 17218–17229, http://dx.doi.org/10.1021/la302331s.

[9] S.R. Khan, S. Ali, B. Ullah, S. Jamil, T. Zanib, Synthesis of iron nanoparticles in poly(N-isopropylacrylamide-acrylic acid) hybrid microgels for catalytic reduction of series of organic pollutants: A first approach, J. Nanoparticle Res. 22 (7) (2020) 72, http://dx.doi.org/10.1007/s11051-020-04924-5.

[10] H.J.M. Wolff, M. Kather, H. Breisig, W. Richtering, A. Pich, M. Wessling, From batch to continuous precipitation polymerization of thermoresponsive microgels, ACS Appl. Mater. Interfaces 10 (29) (2018) 24799–24806, http://dx.doi.org/10.1021/acsami.8b06920.

[11] M. Kather, F. Ritter, A. Pich, Surfactant-free synthesis of extremely small stimuli-responsive colloidal gels using a confined impinging jet reactor, Chem. Eng. J. 344 (2018) 375–379, http://dx.doi.org/10.1016/j.cej.2018.03.082.

[12] P. Fandrich, L. Wiehemeier, M. Dirksen, O. Wrede, T. Kottke, T. Hellweg, Acrylamide precipitation polymerization in a continuous flow reactor: An in situ FTIR study reveals kinetics, Colloid Polym. Sci. 299 (2) (2020) 221–232, http://dx.doi.org/10.1007/s00396-020-04762-w.

[13] L.F. Kaven, H.J.M. Wolff, L. Wille, M. Wessling, A. Mitsos, J. Viell, In-line monitoring of microgel synthesis: Flow versus batch reactor, Org. Process Res. Dev. 25 (9) (2021) 2039–2051, http://dx.doi.org/10.1021/acs.oprd.1c00087.

[14] P. Fandrich, J. Esteban Vázquez, R. Haverkamp, T. Hellweg, Growth of smart microgels in a flow reactor scrutinized by in-line SAXS, Langmuir : ACS J. Surf. Colloids (2023) http://dx.doi.org/10.1021/acs.langmuir.2c02796.

[15] F.A.L. Janssen, M. Kather, A. Ksiazkiewicz, A. Pich, A. Mitsos, Synthesis of poly(N-vinylcaprolactam)-based microgels by precipitation polymerization: Pseudo-bulk model for particle growth and size distribution, ACS Omega 4 (9) (2019) 13795–13807, http://dx.doi.org/10.1021/acsomega.9b01335.

[16] F. Jung, A. Ksiazkiewicz, A. Mhamdi, A. Pich, A. Mitsos, Model-based prediction of the hydrodynamic radius of collapsed microgels and experimental validation, Chem. Eng. J. 378 (8) (2019) 121740, http://dx.doi.org/10.1016/j.cej.2019.05.101.

[17] T. Hoare, D. McLean, Kinetic prediction of functional group distributions in thermosensitive microgels, J. Phys. Chem. B 110 (41) (2006) 20327–20336, http://dx.doi.org/10.1021/jp0643451.

[18] F.A.L. Janssen, M. Kather, L.C. Kröger, A. Mhamdi, K. Leonhard, A. Pich, A. Mitsos, Synthesis of poly(N-vinylcaprolactam)-based microgels by precipitation polymerization: Process modeling and experimental validation, Ind. Eng. Chem. Res. 56 (49) (2017) 14545–14556, http://dx.doi.org/10.1021/acs.iecr.7b03263.

[19] F.A. Janssen, A. Ksiazkiewicz, M. Kather, L.C. Kröger, A. Mhamdi, K. Leonhard, A. Pich, A. Mitsos, Kinetic modeling of precipitation terpolymerization for functional microgels, in: 28th European Symposium on Computer Aided Process Engineering, in: Computer Aided Chemical Engineering, vol. 43, Elsevier, 2018, pp. 109–114, http://dx.doi.org/10.1016/B978-0-444-64235-6.50021-8.

[20] F. Jung, A. Ksiazkiewicz, A. Mhamdi, A. Pich, A. Mitsos, Model-based prediction of the hydrodynamic radius of collapsed microgels and experimental validation, Chem. Eng. J. 378 (2019) 121740, http://dx.doi.org/10.1016/j.cej.2019.05.101.

[21] E. Bradford, A.M. Schweidtmann, A. Lapkin, Efficient multiobjective optimization employing Gaussian processes, spectral sampling and a genetic algorithm, J. Global Optim. 71 (2) (2018) 407–438, http://dx.doi.org/10.1007/s10898-018-0609-2.

[22] W.R. Thompson, On the likelihood that one unknown probability exceeds another in view of the evidence of two samples, Biometrika 25 (3/4) (1933) 285, http://dx.doi.org/10.2307/2332286.

[23] J. Snoek, H. Larochelle, R.P. Adams, Practical Bayesian optimization of machine learning algorithms, in: F. Pereira, C. Burges, L. Bottou, K. Weinberger (Eds.), in: Advances in Neural Information Processing Systems, vol. 25, Curran Associates, Inc., 2012, URL https://proceedings.neurips.cc/paper_files/paper/2012/file/05311655a15b75fab86956663e1819cd-Paper.pdf.

[24] R. Garnett, Bayesian Optimization, Cambridge University Press, 2023.

[25] B.J. Shields, J. Stevens, J. Li, M. Parasram, F. Damani, J.I.M. Alvarado, J.M. Janey, R.P. Adams, A.G. Doyle, Bayesian reaction optimization as a tool for chemical synthesis, Nature 590 (7844) (2021) 89–96, http://dx.doi.org/10.1038/s41586-021-03213-y.

[26] A.M. Schweidtmann, A.D. Clayton, N. Holmes, E. Bradford, R.A. Bourne, A.A. Lapkin, Machine learning meets continuous flow chemistry: Automated optimization towards the Pareto front of multiple objectives, Chem. Eng. J. 352 (1–9) (2018) 277–282, http://dx.doi.org/10.1016/j.cej.2018.07.031.

[27] S. Sano, T. Kadowaki, K. Tsuda, S. Kimura, Application of Bayesian optimization for pharmaceutical product development, J. Pharm. Innov. 15 (3) (2020) 333–343, http://dx.doi.org/10.1007/s12247-019-09382-8.

[28] Y. Naito, M. Kondo, Y. Nakamura, N. Shida, K. Ishikawa, T. Washio, S. Takizawa, M. Atobe, Bayesian optimization with constraint on passed charge for multiparameter screening of electrochemical reductive carboxylation in a flow microreactor, Chem. Commun. (Cambridge, England) 58 (24) (2022) 3893–3896, http://dx.doi.org/10.1039/d2cc00124a.

[29] A. Mogilicharla, P. Mittal, S. Majumdar, K. Mitra, Kriging surrogate based multi-objective optimization of bulk vinyl acetate polymerization with branching, Mater. Manuf. Process. 30 (4) (2015) 394–402, http://dx.doi.org/10.1080/10426914.2014.921709.

[30] W. McPhee, K.C. Tam, R. Pelton, Poly(N-isopropylacrylamide) latices prepared with sodium dodecyl sulfate, J. Colloid Interface Sci. 156 (1) (1993) 24–30, http://dx.doi.org/10.1006/jcis.1993.1075.

[31] X. Wu, R.H. Pelton, A.E. Hamielec, D.R. Woods, W. McPhee, The kinetics of poly(N-isopropylacrylamide) microgel latex formation, Colloid Polym. Sci. 272 (4) (1994) 467–477, http://dx.doi.org/10.1007/BF00659460.

[32] M. Andersson, S.L. Maunu, Structural studies of poly(n-isopropylacrylamide) microgels: Effect of SDS surfactant concentration in the microgel synthesis, J. Polym. Sci. Part B: Polym. Phys. 44 (23) (2006) 3305–3314, http://dx.doi.org/10.1002/polb.20971.

[33] B. Wedel, T. Brändel, J. Bookhold, T. Hellweg, Role of anionic surfactants in the synthesis of smart microgels based on different acrylamides, ACS Omega 2 (1) (2017) 84–90, http://dx.doi.org/10.1021/acsomega.6b00424.

[34] K. von Nessen, M. Karg, T. Hellweg, Thermoresponsive poly-(N-isopropylmethacrylamide) microgels: Tailoring particle size by interfacial tension control, Polymer 54 (21) (2013) 5499–5510, http://dx.doi.org/10.1016/j.polymer.2013.08.027.

[35] O.L.J. Virtanen, W. Richtering, Kinetics and particle size control in non-stirred precipitation polymerization of N-isopropylacrylamide, Colloid Polym. Sci. 292 (8) (2014) 1743–1756, http://dx.doi.org/10.1007/s00396-014-3208-x.

[36] A. Balaceanu, D.E. Demco, M. Möller, A. Pich, Microgel heterogeneous morphology reflected in temperature-induced volume transition and 1 h high-resolution transverse relaxation NMR. The case of poly(N-vinylcaprolactam) microgel, Macromolecules 44 (7) (2011) 2161–2169, http://dx.doi.org/10.1021/ma200103y.

[37] F. Schneider, A. Balaceanu, A. Feoktystov, V. Pipich, Y. Wu, J. Allgaier, W. Pyckhout-Hintzen, A. Pich, G.J. Schneider, Monitoring the internal structure of poly(N-vinylcaprolactam) microgels with variable cross-link concentration, Langmuir : ACS J. Surf. Colloids 30 (50) (2014) 15317–15326, http://dx.doi.org/10.1021/la503830w.

[38] O.L.J. Virtanen, M. Kather, J. Meyer-Kirschner, A. Melle, A. Radulescu, J. Viell, A. Mitsos, A. Pich, W. Richtering, Direct monitoring of microgel formation during precipitation polymerization of N-isopropylacrylamide using in situ SANS, ACS Omega 4 (2) (2019) 3690–3699, http://dx.doi.org/10.1021/acsomega.8b03461.

[39] A. Imaz, J. Forcada, N-vinylcaprolactam-based microgels: Synthesis and characterization, J. Polym. Sci. A 46 (7) (2008) 2510–2524, http://dx.doi.org/10.1002/pola.22583.

[40] Y.Y. Chiu, L.J. Lee, Microgel formation in the free radical crosslinking polymerization of ethylene glycol dimethacrylate (EGDMA). I. Experimental, J. Polym. Sci. A 33 (2) (1995) 257–267, http://dx.doi.org/10.1002/pola.1995.080330208.

[41] D. Bongartz, J. Najman, S. Sass, A. Mitsos, MAiNGO - McCormick-based algorithm for mixed-integer nonlinear global optimization. Technical report, 2018, URL https://www.avt.rwth-aachen.de/global/show_document.asp?id=aaaaaaaaabclahw.

[42] A.M. Schweidtmann, D. Bongartz, D. Grothe, T. Kerkenhoff, X. Lin, J. Najman, A. Mitsos, Deterministic global optimization with Gaussian processes embedded, Math. Program. Comput. 13 (3) (2021) 553–581, http://dx.doi.org/10.1007/s12532-021-00204-y.

[43] E. Kriesten, F. Alsmeyer, A. Bardow, W. Marquardt, Fully automated indirect hard modeling of mixture spectra, Chemometr. Intell. Lab. Syst. 91 (2) (2008) 181–193, http://dx.doi.org/10.1016/j.chemolab.2007.11.004.

[44] L. Kaven, H. Wolff, L. Wille, M. Wessling, A. Mitsos, J. Viell, Dataset to: Inline monitoring of microgel synthesis: Flow versus batch reactor, 2021, http://dx.doi.org/10.18154/RWTH-2021-09666.

[45] L. Kaven, A.M. Schweidtmann, J. Keil, J. Israel, N. Wolter, A. Mitsos, Dataset to: Data-driven product-process optimization of N-isopropylacrylamide microgel flow-synthesis, 2023, http://dx.doi.org/10.18154/RWTH-2023-05551.

[46] Sigma-Aldrich Chemie GmbH, Safety data sheet 440914. version 7.2, 2023, URL https://www.sigmaaldrich.com/DE/en/sds/aldrich/440914.

[47] M. Ehrgott, Multiobjective optimization, AI Mag. 29 (4) (2009) 47, http://dx.doi.org/10.1609/aimag.v29i4.2198.

[48] E. Bradford, TS-EMO algorithm. https://github.com/Eric-Bradford/TS-EMO, last updated 2020-06.

[49] D. Bongartz, MAiNGO - McCormick-based algorithm for mixed-integer nonlinear global optimization. https://git.rwth-aachen.de/avt-svt/public/maingo, last updated 2021-06.

[50] A. Schweidtmann, MeLOn - Machine learning models for optimization, 2021, https://git.rwth-aachen.de/avt-svt/public/MeLOn, last updated 2021-06.